Virtual Conductance Based Cascade Voltage Controller for VSCs in Islanded Operation Mode

Francisco Jesús Matas-Díaz, Manuel Barragán-Villarejo, Juan Carlos Olives-Camps, Juan Manuel Mauricio, and José María Maza-Ortega

***Abstract*—Voltage source converters have become the main enabler for the integration of distributed energy resources in microgrids. In the case of islanded operation, these devices normally set the amplitude and frequency of the network voltage by means of a cascade controller composed of an outer voltage control loop and an inner current control loop. Several strategies to compute the gains of both control loops have been proposed in the literature in order to obtain a fast and decoupled response of the voltages at the point of common coupling. This paper proposes an alternative and simple methodology based on the introduction of a virtual conductance in the classic cascade control. This strategy allows to design each control loop independently, obtaining a closed-loop response of a first-order system. In this way, the gains of each control loop are easily derived from the parameters of the LC coupling filter and the desired closed-loop time constants. Furthermore, a state observer is included in the controller to estimate the inductor current of the LC filter in order to reduce the number of required measurements. A laboratory testbed is used to validate and compare the proposed controller. The experimental results demonstrate the effectiveness of the proposal both in steady-state and transient regimes.**

***Index Terms*—Voltage source converter, microgrid, cascade controller tuning, virtual conductance.**

I. Introduction

THE success of the integration of distributed renewable energy sources (DRESs), electrical vehicles or energy storage systems is largely linked to the development of power electronics [1]. In particular, the voltage source converter (VSC) is of utmost importance nowadays because it provides an efficient and flexible interface between the DC resources with the AC network [2]. VSCs may bring a plethora of functionalities for improving the power system operation and pushing towards a fully decarbonized scenario in the near future. For this reason, VSC control algorithms have evolved during the last decades according to the demanded requirements of each application. In case of conventional power systems, where synchronous machines are responsible of maintaining the voltage and the frequency, most of the VSCs operate in grid-feeding mode [3]. These VSCs are controlled as current sources which require a synchronisation with the power grid for injecting the active and reactive power references. Conversely, in the case of islanded systems, the VSCs are operated as voltage sources because it is required to form an AC grid, i.e., to define the frequency and voltage amplitudes of the power system. Nevertheless, during the last years, the grid-forming concept is widely discussed for grid-connected applications because of the need of enhancing the DRES functionalities when the conventional synchronous generation is being displaced by this new technology. An interesting discussion about the evolution of the terminology and VSC characterization can be found in [4].

Grid-forming VSCs are composed of different control layers which can be integrated in a hierarchical manner. In the case of grid-connected applications or islanded microgrids with more than one VSC, a higher control layer is required for defining the frequency and voltage amplitudes to achieve a set of functionalities. With this regard, different techniques relying on droop controllers for active and reactive power sharing [5], advanced algorithms mimicking the dynamic performance of a synchronous generator [6] or even minimizing the subsynchronous oscillations in power systems [7] have been proposed. Then, a voltage controller is applied to track the computed voltage reference. On the contrary, in the case of a single VSC supplying an islanded system, only a voltage controller to set the desired voltage reference (amplitude and frequency) is required without the need to implement the higher control layer.

Focusing on the voltage controller, which is the main objective of this paper, two possible alternatives have been applied for grid-connected and islanded applications: single voltage control loop or cascade voltage control loops.

The former methods control the voltage at point of common coupling (PCC) directly through a single control loop based on state feedback as presented in [8]-[10]. The main challenge of this type of controllers is to deal with overcur-

Manuscript received: February 14, 2021; revised: July 28, 2021; accepted: April 7, 2022. Date of CrossCheck: April 7, 2022. Date of online publication: July 15, 2022.

This work was supported by the European Union Horizon 2020 under grant agreement 764090 (EASY-RES), Spanish Ministry of Economy under grant ENE2017-84813-R and CERVERA Research Programme of CDTI, the Industrial and Technological Development Centre of Spain, under the research project HySGrid+(CER-20191019), and in part by Universidad de Sevilla in the framework of VI PPIT-US.

F. J. Matas-Díaz, M. Barragán-Villarejo, J. C. Olives-Camps, J. M. Mauricio, and J. M. Maza-Ortega (corresponding author) are with the Department of Electrical Engineering, Universidad de Sevilla, Seville 41092, Spain (e-mail: fmatas@us.es; manuelbarragan@us.es; jolives@us.es; j.m.mauricio@ieee.org; jmmaza@us.es).

DOI: 10.35833/MPCE.2021.000121

rent situations as the current control loop is fully removed [11]. To solve this problem, the PCC reference voltage can be modified according to the VSC current using a voltage droop characteristic [8] or by means of a threshold virtual impedance [10].

Despite the good performance offered by these single-loop strategies, even in case of overcurrent situations, cascade control loops are also a popular alternative widely used in series-connected and grid-forming VSCs. These algorithms are based on an outer control loop (OCL) and an inner control loop (ICL) in charge of controlling the voltage and current, respectively [12]-[17]. Conventionally, the ICL and the OCL are based on proportional integral (PI) controllers formulated on a rotating synchronous frame and designed with sufficient separation between their corresponding bandwidths in such a way that their dynamics do not interact with each other [18]. To achieve this goal, the ICL is tuned faster than the OCL, allowing an independent controller design. Probably, this is the reason why cascade controllers are widely used. However, despite the apparent ease of this control strategy, an adequate computation of the controller gains to guarantee the time constants of each control loop is not straightforward due to the characteristics of the plants to be controlled. Thus, the use of PI controllers in the ICL with proportional controllers in the OCL is proposed in [12] at the cost of a steady-state error at the voltage of PCC. This error can be eliminated by introducing a proportional resonant (PR) controller in the outer voltage control loop. However, it is required to use a quite small cutoff frequency to avoid introducing a phase shift towards the crossover frequency which decreases the phase margin and leads to a slow dynamics. Recently, a sliding-mode control for the ICL and a mixed H_2/H_∞ for the OCL have also been proposed [13]. In this way, a robust controller without a precise model of the VSC and its coupling filter can be obtained. Nevertheless, this complex technique is suitable for VSCs operating with low-switching frequencies where the possible resonances with the power system must be damped. Other sophisticated control techniques such as predictive control [19] or neural networks [20] have been reported. Despite the good performance of these proposals, it has to be considered that the controller tuning relies on some auxiliary processes, i.e., the selection of adequate weighting factors of the cost function for the predictive controllers or training stages in the case of neural networks. Finally, an interesting interpretation of the controllers used in grid-forming VSCs as circuit elements has been recently outlined in [21], giving clues of the role of each controller parameter on the overall system performance.

This paper proposes to modify the classic cascade voltage control of a single LC-coupled grid-forming VSC operating in islanded mode by adding a negative feedback through a virtual conductance at the PCC. This allows to design the voltage and current control loops independently so that they respond following a given first-order closed-loop time constants with guaranteed system stability. The capacitor voltage and the injected PCC current are used as measurements in the control algorithm due to their low content of switching harmonics. Therefore, the inductor-side current of the VSC is unknown, preventing the application of a cascade controller. In order to apply the proposed cascade control strategy, a state observer to estimate this current is implemented. In this way, the number of current sensors is reduced while the control algorithm benefits from a filtered inductor-side current estimation with reduced harmonic content.

The rest of this paper is organized as follows. Section II-A and II-B present the mathematical model of the LC-coupled VSC and the classic cascade control algorithm, respectively. After that, the proposed virtual conductance and the tuning of the OCL gains are presented. Section III outlines a sensitivity analysis where the influence of the virtual conductance value and controller time constant are evaluated using a frequency domain and stability analyses. Section IV describes the experimental results obtained in the laboratory to validate the proposed virtual conductance technique. The controller performance is analyzed for steady-state and transient test cases, including a step change in the load and a large perturbation to evaluate the performance of the proposed controller. This paper closes with the main conclusions and future research lines.

II. Theoretical Framework

This section is devoted to give the details of the proposed control algorithm based on a virtual conductance in parallel with the filter capacitor. For this purpose, the averaged model of the LC-coupled VSC is presented first, followed by the definition of the virtual conductance which allows a simplified tuning of the cascade controller gains. The section closes with the formulation of the complete control algorithm including the cross-coupling cancellation terms and a state observer for estimating the filter inductor current.

A. Averaged Model of LC-coupled VSC

This subsection details the averaged model of an LC-coupled VSC, as shown in Fig. 1, in *abc* coordinates and its corresponding counterpart in *dq* rotating reference frame.

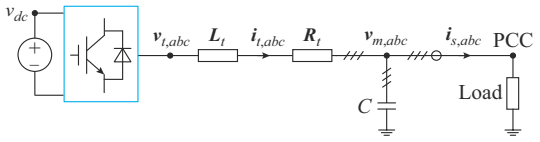

Fig. 1. One-line diagram of an LC-coupled VSC connected to an islanded system.

It is assumed that the DC side of VSC is connected to a constant DC voltage source. Therefore, the differential equations related to this system in the *abc* coordinates are defined as [22]:

$$\boldsymbol{v}_{t,abc} = \boldsymbol{R}_t \boldsymbol{i}_{t,abc} + \boldsymbol{L}_t \frac{\mathrm{d}\boldsymbol{i}_{t,abc}}{\mathrm{d}t} + \boldsymbol{v}_{m,abc} \tag{1}$$

$$\boldsymbol{i}_{t,abc} = \boldsymbol{C} \frac{\mathrm{d}\boldsymbol{v}_{m,abc}}{\mathrm{d}t} + \boldsymbol{i}_{s,abc} \tag{2}$$

where $\boldsymbol{v}_{t,abc} = [\,v_{ta} \quad v_{tb} \quad v_{tc}\,]^{\mathrm{T}}$ is the VSC terminal voltage; $\boldsymbol{v}_{m,abc} = [\,v_{ma} \quad v_{mb} \quad v_{mc}\,]^{\mathrm{T}}$ is the capacitor voltage; $\boldsymbol{i}_{t,abc} = [\,i_{ta} \quad i_{tb} \quad i_{tc}\,]^{\mathrm{T}}$ is the inductor current; $\boldsymbol{i}_{s,abc} = [\,i_{sa} \quad i_{sb} \quad i_{sc}\,]^{\mathrm{T}}$ is the injected PCC current; and the LC coupling filter is rep-

resented by the diagonal matrices $\boldsymbol{L}_t=\text{diag}[L_t \quad L_t \quad L_t]$, $\boldsymbol{R}_t=\text{diag}[R_t \quad R_t \quad R_t]$, and $\boldsymbol{C}=\text{diag}[C \quad C \quad C]$.

These equations can be transformed into the *dq* coordinates by using the Park transformation as:

$$\boldsymbol{v}_{t,dq}=\boldsymbol{R}_{t,dq}\boldsymbol{i}_{t,dq}+\boldsymbol{L}_{t,dq}\frac{\mathrm{d}\boldsymbol{i}_{t,dq}}{\mathrm{d}t}+\omega\boldsymbol{L}_{t,dq}\boldsymbol{i}_{t,qd}+\boldsymbol{v}_{m,dq} \tag{3}$$

$$\boldsymbol{i}_{t,dq}=\boldsymbol{C}_{dq}\frac{\mathrm{d}\boldsymbol{v}_{m,dq}}{\mathrm{d}t}+\omega\boldsymbol{C}_{dq}\boldsymbol{v}_{m,qd}+\boldsymbol{i}_{s,dq} \tag{4}$$

where the vectors with subscripts *d* and *q* correspond to voltages and currents in *dq* coordinates; ω is the angular frequency; $\boldsymbol{L}_{t,dq}=\text{diag}[-L_t \quad L_t]$; $\boldsymbol{R}_{t,dq}=\text{diag}[R_t \quad R_t]$; and $\boldsymbol{C}_{dq}=\text{diag}[-C \quad C]$.

B. Cascade Control Algorithm

The classic cascade voltage controller for an LC-coupled VSC on a rotating synchronous frame is represented in Fig. 2. In order to simplify the addition of the virtual conductance and the computation of the controller gains, the cross-coupling cancellation terms of (3) have been omitted in the analysis. Note that this simplification leads to the same dynamic system for *dq* coordinates. The objective of this strategy is to control the PCC voltage through the capacitor voltage v_m. For this purpose, two cascade PI controllers, i. e., ICL and OCL, are applied. On the one hand, the OCL generates the reference current i_t^* to the ICL. On the other hand, the ICL generates the voltage v_t at the VSC terminals to track the reference voltage v_m^*. Usually, dynamics of the OCL is assumed to be much slower than that of the ICL. This assumption allows to design each control loop independently without considering the mutual dynamic interactions [14]. Nevertheless, it has to be considered that this dynamic separation of the controllers requires a high bandwidth of the inner current control loop and a high-switching frequency of the VSC.

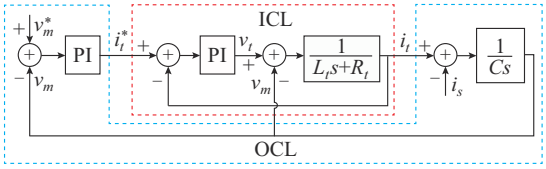

Fig. 2. Simplified block diagram of the classic cascade voltage controller for an LC-coupled VSC on the rotating synchronous frame.

Taking into account these issues, the ICL PI controller can be designed considering just its action on the inductive filter. This plant, composed of R_t and L_t as shown in Fig. 2, presents a first-order dynamics. In this case, the controller gains can be easily computed as [22]:

$$\begin{cases} k_{p,i}=\dfrac{L_t}{\tau_i} \\ k_{i,i}=\dfrac{R_t}{\tau_i} \end{cases} \tag{5}$$

where $k_{p,i}$ and $k_{i,i}$ are the proportional and the integral gains of the PI controller, respectively; and τ_i is the desired ICL time constant. The use of these controller gains leads to a controlled closed-loop response following a first-order dynamics with τ_i.

The same simplification can be applied to the OCL design which leads to consider that i_t equals i_t^*. In this way, the OCL PI controller is applied directly to a plant composed of the capacitor C as shown in Fig. 3(a). The computation of the control gains in this case is not straightforward because, as stated in the introduction section, the closed-loop system has a second-order dynamics. Its tuning requires to adjust the damping ratio and natural frequency by means of modifying the control gains, and the system would provide a typical second-order response with a certain rise time, overshoot and settle time depending on the damping coefficient and natural frequency. The next subsection presents how the incorporation of a virtual conductance in the classical cascade control solves this shortcoming and facilitates the computation of the OCL gains.

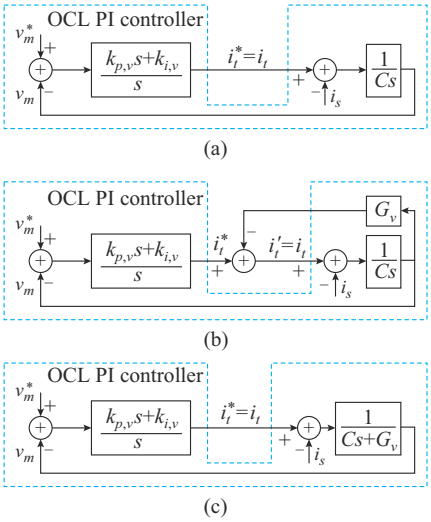

Fig. 3. Simplified block diagrams of OCL within a cascade voltage controller for an LC-coupled VSC simplifying ICL dynamics. (a) OLC PI controller and plant. (b) OCL PI controller and plant including the negative feedback of the virtual conductance G_v. (c) OCL PI controller and plant in a compact form.

C. Virtual Conductance and Tuning of OCL Gains

The main idea is to modify the original control algorithm shown in Fig. 3(a), where the ICL dynamics has been ommited, by including the negative feedback of G_v. This modifies the ICL reference current as shown in Fig. 3(b). This negative feedback can be transformed using block diagram operations as shown in Fig. 3(c). In this way, the OCL PI controller is applied to a plant with a first-order dynamics which facilitates the computation of the controller gains:

$$\begin{cases} k_{p,v}=\dfrac{C}{\tau_v} \\ k_{i,v}=\dfrac{G_v}{\tau_v} \end{cases} \tag{6}$$

where $k_{p,v}$ and $k_{i,v}$ are the proportional and the integral gains of the OCL PI controller, respectively; and τ_v is the desired OCL time constant. These gains guarantee a first-order dynamics of the closed-loop system with τ_v in a similar way than those in the ICL case.

D. Proposed Control Algorithm with Virtual Conductance

The complete control algorithm in *dq* coordinates including the virtual conductance is shown in Fig. 4. The ICL is in charge of computing the VSC voltage reference $\boldsymbol{v}_{t,dq}$ as:

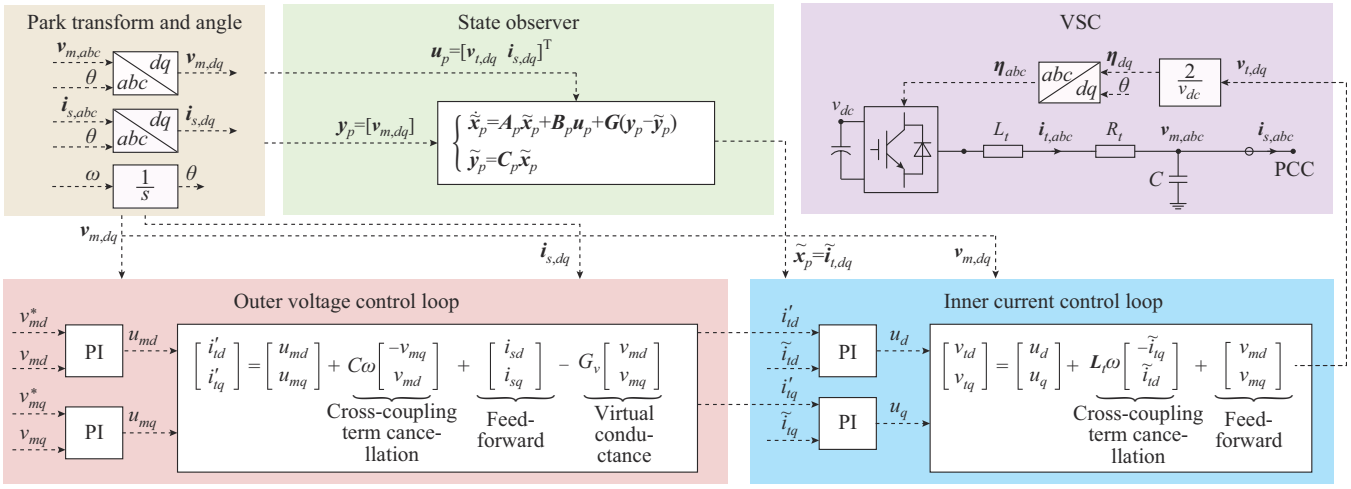

Fig. 4. Proposed cascade control with virtual conductance in *dq* coordinates for grid-forming LC-coupled VSCs.

$$\boldsymbol{v}_{t,dq}=k_{p,i}\boldsymbol{e}_{i_{t,dq}}+k_{i,i}\boldsymbol{\xi}_{i_{t,dq}}+\omega\boldsymbol{L}_{t,dq}\tilde{\boldsymbol{i}}_{t,qd}+\boldsymbol{v}_{m,dq} \tag{7}$$

where $\boldsymbol{e}_{i_{t,dq}}$ and $\boldsymbol{\xi}_{i_{t,dq}}$ are the error and the integral error of the estimated inductor current $\tilde{\boldsymbol{i}}_{t,dq}$, respectively.

Note that it is proposed to estimate the inductor current $\tilde{\boldsymbol{i}}_{t,dq}$, given $\boldsymbol{v}_{m,dq}$ and the injected PCC current $\boldsymbol{i}_{s,dq}$, following the methodology summarised in Appendix A.1 [8]. This strategy provides some advantages with respect to directly use the measured inductor current $\boldsymbol{i}_{t,abc}$. First, the high-frequency harmonic distortion due to the VSC switching is lower in the injected PCC current due to the LC filter action. This prevents the introduction of a noisy signal in the controller. With this regard, it has to be considered that the effectiveness of the synchronized sampling is limited when non-ideal conditions are considered [23], e.g., non-linear evolution of the current within the switching period or the delays introduced by drivers and insulated gate bipolar transistors (IGBTs). Second, the control algorithm is intended to track the capacitor voltage $\boldsymbol{v}_{m,abc}$ to a given voltage reference while the injected PCC current $\boldsymbol{i}_{s,abc}$ is considered as a system disturbance. For this reason, the measurement of this current is one of the most efficient ways to reject it. Note that the VSC inductor current is affected by the capacitor dynamics. Therefore, when a rapid change in $\boldsymbol{i}_{s,abc}$ occurs, e.g., due to a short-circuit fault, the inductor current $\boldsymbol{i}_{t,abc}$ will experience a delay which may affect the controller performance.

The ICL reference current $\boldsymbol{i}'_{t,dq}$ is computed by the OCL as:

$$\boldsymbol{i}^{*}_{t,dq}=k_{p,v}\boldsymbol{e}_{v_{m,dq}}+k_{i,v}\boldsymbol{\xi}_{v_{m,dq}}+\omega\boldsymbol{C}_{dq}\boldsymbol{v}_{m,qd}+\boldsymbol{i}_{s,dq} \tag{8}$$

$$\boldsymbol{i}'_{t,dq}=\boldsymbol{i}^{*}_{t,dq}-G_v\boldsymbol{v}_{m,dq} \tag{9}$$

where $\boldsymbol{e}_{v_{m,dq}}$ and $\boldsymbol{\xi}_{v_{m,dq}}$ are the error and the integral error of the capacitor voltage $\boldsymbol{v}_{m,dq}$, respectively; and $\boldsymbol{i}^{*}_{t,dq}$ is the reference current in the classic cascade control while $\boldsymbol{i}'_{t,dq}$ modifies it with the proposed virtual conductance.

III. Sensitivity Analysis

The aim of this section is to evaluate the influence of the introduced virtual conductance in the system dynamics in order to define its adequate value. First, the plant in which the OCL applies its control action resorting to a transfer function analysis is considered. Second, a stability analysis is conducted to guarantee that the computed controller gains and the introduced virtual conductance lead to a stable closed-loop operation.

For this purpose, the proposed control algorithm is applied to a VSC with the characteristics summarized in Table I. Note that the VSC parameters are expressed in per unit to obtain general conclusions irrespective of the converter rated magnitudes. The analysis includes a wide range of virtual conductances and ICL time constants but assumes $\tau_v=10\tau_i$.

TABLE I
VSC and Controller Parameters Used in Sensitivity Analysis

Parameter	Value
L_t	0.2 p.u.
R_t	0.02 p.u.
C	8×10^{-6} p.u.
G_v	$[0.04, 0.16, 0.4, 0.8, 4.0, 8.0]$ p.u.
τ_i	$[0.25, 0.5, 1.0, 5.0, 10.0, 50.0]$ ms
τ_v	$\tau_v=10\tau_i$

A. Transfer Function Analysis

The proposed tuning of the OCL gain detailed in Section II-C neglects the ICL dynamics. The aim of this subsection is to validate this assumption by comparing the frequency domain performance of the complete and simplified plants shown in Fig. 2 and Fig. 3(c), respectively. The corresponding transfer functions G_{wICL} and G_{woICL} are:

$$\begin{cases} G_{wICL}=\dfrac{k_{p,i}s+k_{i,i}}{s(s^2+2\delta\omega_n s+\omega_n^2)+k_{i,i}G_v} \\ G_{woICL}=\dfrac{1}{Cs+G_v} \end{cases} \tag{10}$$

$$\begin{cases} \omega_n = \sqrt{\dfrac{1+k_{p,i}G_v+k_{i,i}C}{L_tC}} \\ \delta = \dfrac{R_t+k_{p,i}}{2L_t\omega_n} \end{cases} \tag{11}$$

where ω_n and δ are the resonance frequency and damping factor of G_{wICL}, respectively.

The representation of the transfer functions in the frequency domain is shown in Fig. 5, where $\tau_i = 0.25$ ms and the extreme values of the virtual conductance (0.04 p.u. and 8 p.u.) have been used. Note that the control strategy is implemented in *dq* coordinates where time-invariant setpoints are DC magnitudes. With this regard, the magnitude and phase of both transfer functions coincide in the low-frequency range (lower than 10 rad/s) for any G_v. This means that the simplification of the dynamics used in the tuning of OCL gain is valid, as the dynamic performance of both plants is identical for low frequencies close to DC. The analysis of the high-frequency range reveals the magnitude drops of 20 dB and 40 dB per decade corresponding to the first- and second-order dynamics of G_{wICL} and G_{woICL}, respectively.

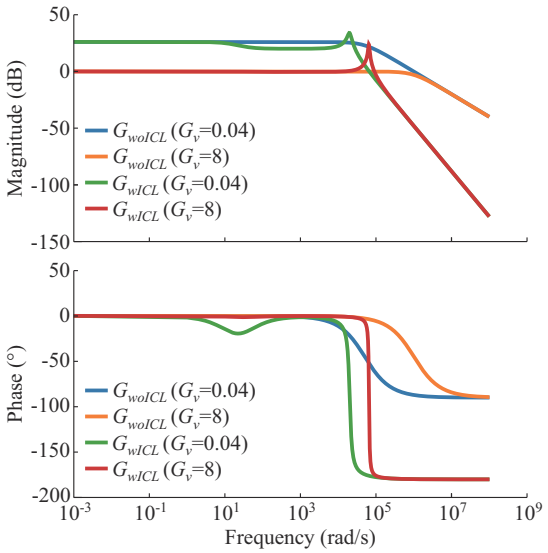

Fig. 5. Transfer function analysis of OCL acting on simplified and complete plants with different values of G_v.

The influence of the virtual conductance value is also evident when a comparison of the transfer functions is carried out. Small values of virtual conductance lead to higher magnitudes in the low-frequency range but with a small drop below the resonance frequency. This means that the controller will be able to reach zero steady-state errors but some deviations with respect to the first-order dynamics for frequencies below the resonance frequency are expected. On the contrary, large values of virtual conductance lead to extremely low magnitudes. Therefore, the controller is expected to have large steady-state errors. The increase of the OCL gains could solve this situation but at the cost of reducing τ_v which may approach τ_i. Therefore, interactions between ICL and OCL may appear. Furthermore, a high value of G_v increases the resonance frequency of the system and reduces the damping factor as shown in (11) and Fig. 5. This situation must be avoided in order to push the resonance frequency far from the switching frequency of the VSC.

B. Stability Analysis

The aim of this subsection is to evaluate the impact of the introduced virtual conductance and the controller time constants on the closed-loop system operation. For this purpose, the state-space equations of the system dynamics given by (3) and (4) and the controller formulated in (7) and (8) are derived in the form as:

$$\dot{\boldsymbol{x}} = \boldsymbol{A}\boldsymbol{x} + \boldsymbol{B}\boldsymbol{u} \tag{12}$$

where $\boldsymbol{x} = [\boldsymbol{i}_{t,dq} \quad \boldsymbol{v}_{m,dq} \quad \boldsymbol{\xi}_{i_{t,dq}} \quad \boldsymbol{\xi}_{v_{m,dq}}]^{\mathrm{T}}$ is the vector of state variables; $\boldsymbol{u} = [v^*_{m,dq} \quad i_{s,dq}]^{\mathrm{T}}$ corresponds to the system inputs; and matrices $\boldsymbol{A}$ and $\boldsymbol{B}$ are detailed in Appendix A.2.

First, the influence of the virtual conductance for $\tau_i = 0.25$ ms is evaluated. The representation of the eigenvalues as a function of the virtual conductance is shown in Fig. 6(a). The system is always stable and the low-frequency eigenvalues maintain a damping ratio equal to 100% for any value of virtual conductance. Conversely, high-frequency eigenvalues reduce their damping ratio and increase their natural frequency as the virtual conductance increases, which is consistent with (11). Therefore, large virtual conductance values must be avoided to reduce the amplification of low-order and switching harmonics of the VSC which may reduce the system performance. With this regard, it is considered that acceptable virtual conductance values are those assuring a damping ratio greater than 10% which corresponds to values lower than 0.4 p.u..

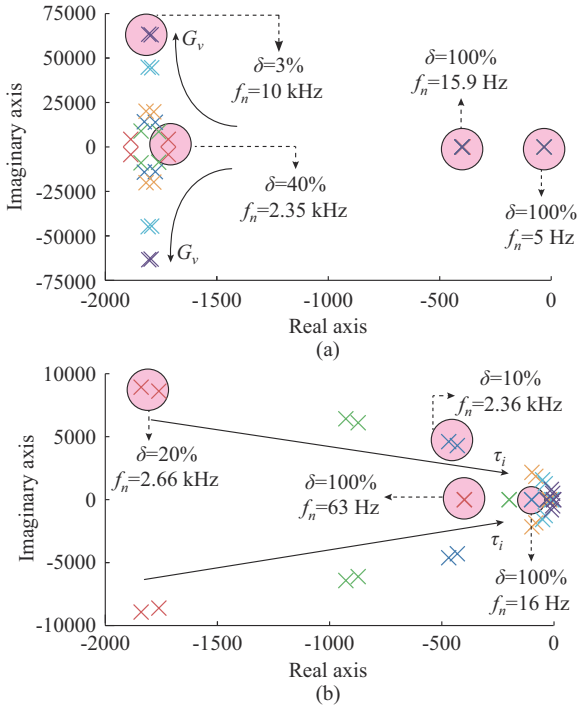

Fig. 6. Stability analysis: eigenvalues of system plant and the proposed controller. (a) Influence of G_v when $\tau_i = 0.25$ ms. (b) Influence of τ_i when $G_v = 0.4$ p.u..

The influence of the ICL time constant has also been evaluated in the stability analysis. In this case, the virtual conductance is set to be 0.4 p.u., while the ICL time constant is modified according to the values shown in Table I. The representation of the eigenvalues in this case is shown in Fig. 6(b). On the one hand, the low-frequency eigenvalues maintain a damping ratio close to 100% and reduce the value of their natural frequency as the value of the ICL time constant increases. On the other hand, the high-frequency eigenvalues reduce the value of their natural frequency and their damping ratio as the ICL time constant increases. Despite the fact that the system stability is guaranteed for any value of the ICL time constant, it is observed that the higher this value, the closer the eigenvalues to the imaginary axis, i.e., critical stable system. With this regard, and as in the case of the discussion on the virtual conductance, it is considered that acceptable values of the ICL time constant are those leading to a damping ratio greater than 10%, which corresponds to values lower than 5 ms.

IV. Experimental Validation

A. Description of Testbed

The experimental setup used to validate the proposed control algorithm is shown in Fig. 7. This testbed consists of a three-phase three-wire VSC with a DC voltage source connected at its DC side which provides the energy to the system. The VSC at AC side is connected to the PCC through an LC filter where different loads have been connected to evaluate the performance of the control algorithm. The relevant parameters of the hardware components and the proposed voltage control strategy are summarized in Tables II and III, respectively.

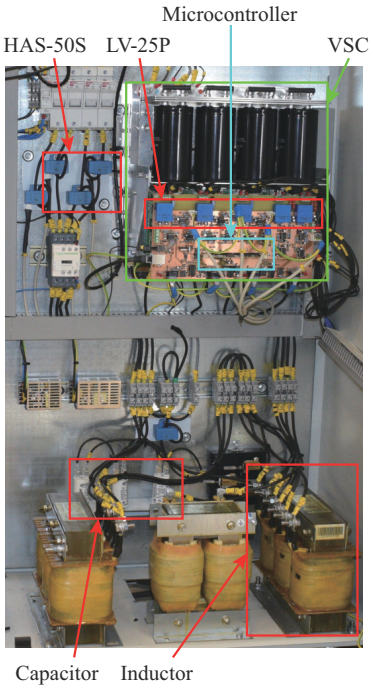

Fig. 7. Laboratory experimental testbed.

TABLE II
Hardware Components of Experimental Testbed

Parameter	Value
DC bus voltage	730 V
VSC rated voltage at AC side	400 V
VSC rated current at AC side	40 A
Rated frequency	50 Hz
Switching frequency	10 kHz
Filter inductor	5 mH
Filter inductor quality factor	100
Filter capacitor	1 μF
LC-filter resonant frequency	2.25 kHz

TABLE III
Parameters of Proposed Control Strategy

Parameter	Value
τ_i	0.25 ms
$k_{p,i}$	20 V/A
$k_{i,i}$	62 V/A
τ_v	2.5 ms
$k_{p,v}$	4×10^{-4} A/V
$k_{i,v}$	4.5 A/V
G_v	0.02 S

The three-phase capacitor voltage $\boldsymbol{v}_{m,abc}$ and the injected PCC current $\boldsymbol{i}_{s,abc}$ are measured using transducers from LEM, LV-25P, and HAS-50S, respectively. The control algorithm shown in Fig. 4 has been implemented on a TMS320F28335 Delfino DSP from Texas Instruments with a sampling frequency of 20 kHz.

B. Experimental Results

The effectiveness of the proposed controller is evaluated experimentally by using the laboratory setup and control parameters defined in the previous subsection. For this purpose, different loads have been connected to the VSC to assess its performance both in steady-state and transient regimes. In both cases, two load conditions have been tested: a three-phase delta resistive balanced load of 42 Ω per phase; no-load. The state observer detailed in Appendix A.1 Section A has been implemented for estimating the inductor current from the injected PCC current. This is an alternative to the synchronous sampling of the inductor current, which prevents the errors due to the non-linear evolution of the current within the switching period and the delays introduced by drivers and IGBTs [23]. Finally, it is important to point out that the second test is quite challenging because no damping of the LC-filter resonance is introduced.

The results obtained in the steady-state test are shown in Fig. 8, where the voltage references are set as $v^*_{md}=0$ V, $v^*_{mq}=-330$ V. It can be observed that an almost perfect sinusoidal waveform is achieved for both load conditions. However, a light superimposed band appears which corresponds to the high-frequency harmonics generated by the VSC switching. In any case, the obtained power quality is excellent because the total harmonic distortion (THD) of the voltage is 1.40%

and 0.91% in the load and no-load tests, respectively.

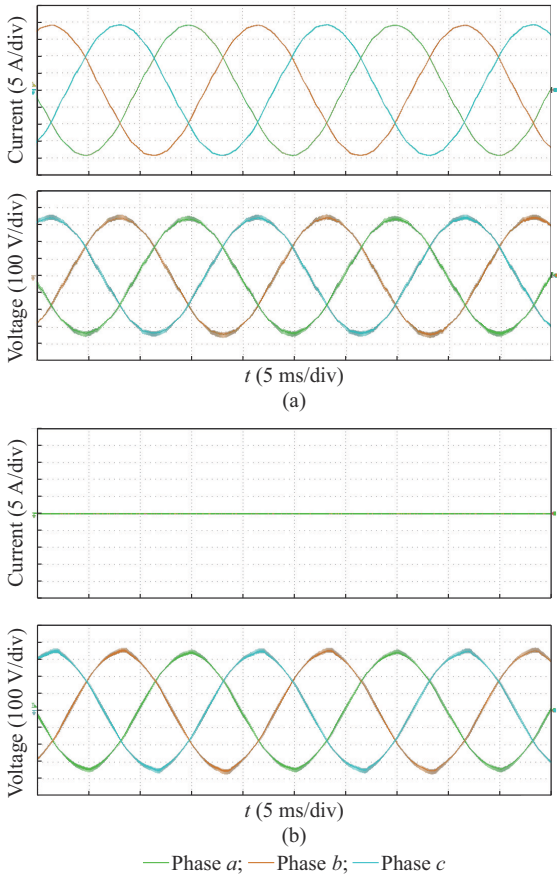

Fig. 8. Steady-state results with $v^*_{md}=0$ V and $v^*_{mq}=-330$ V. (a) Three-phase delta resistive balanced load of 42 Ω per phase. (b) No-load operation.

Regarding the transient performance of the voltage controller, a step change of the voltage references has been tested. The initial voltage setpoint is modified from $v^*_{mq}=0$ V to $v^*_{mq}=-330$ V with the result shown in Fig. 9.

For comparison purposes, it has been included Fig. 9 an exponential function with τ_v. It is worth noting that the voltages evolve following a controlled first-order dynamics as a result of the virtual conductance introduced in the OCL. With this regard, it is interesting to analyze the dynamic performance of the PCC voltages in the *dq* coordinates as shown in Fig. 10. The analysis of this figure evidences two important characteristics of the proposed controller. First, and regarding the *q* component, it can be observed that the voltages follow the desired first-order dynamics with τ_v. Second, a good uncoupling of the *d* and *q* components is achieved as the *d* component is almost constant with the reference change of the *q* component.

C. Performance with Large Perturbation

Finally, the controller is tested in case of a three-phase fault at the PCC in order to evaluate its performance under a large disturbance. This test has been performed using a hardware-in-the-loop (HIL) testing approach on the Typhoon HIL 402-01-005 platform. Therefore, the control algorithm can be safely tested in the microcontroller without jeopardizing the VSC.

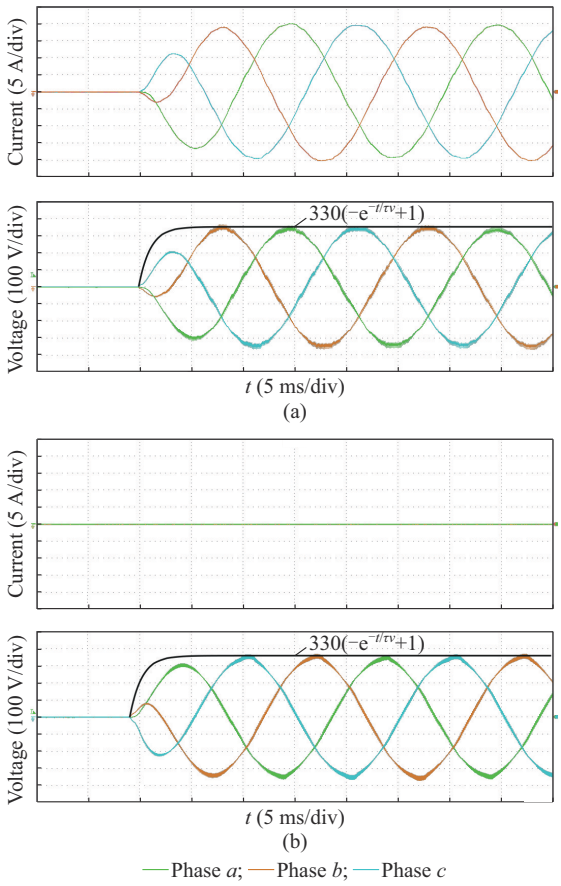

Fig. 9. Transient behaviour when $v^*_{md}=0$ V and $v^*_{mq}=0$ V → −330 V. (a) Three-phase delta resistive balanced load of 42 Ω per phase. (b) No-load operation.

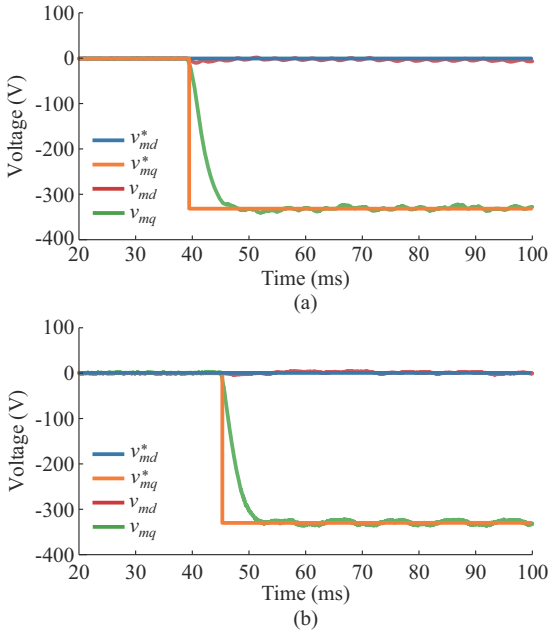

Fig. 10. Voltages in *dq* coordinates for transient behaviour. (a) Three-phase balanced delta resistive load of 42 Ω per phase. (b) No-load operation.

For this purpose, a saturation block between the OCL and the ICL is integrated in the proposed control algorithm shown in Fig. 4. A back-calculation anti-wind-up method has

been implemented to prevent the integration wind-up when the control action is saturated [24]. The current limits for each d and q components is set to be ±20 A in order to protect the VSC against overcurrents. In any case, these values can be modified depending on the VSC rated power or the corresponding protection criteria.

Figure 11 represents the magnitudes $\boldsymbol{v}_{m,abc}$, $\boldsymbol{i}_{s,abc}$, and $\boldsymbol{i}_{t,abc}$ during this short-circuit fault test. The fault starts at $t=0.1$ s and ends at $t=0.22$ s. During the fault, the voltage is practically zero but once the fault is cleared, the voltage recovers its previous reference with a slight overvoltage during a short transient period. With respect to the current, it is important to point out that $\boldsymbol{i}_{t,abc}$ is maintained within the imposed limits without any unwanted overcurrent which could lead to a VSC damage. Note that the injected PCC current $\boldsymbol{i}_{s,abc}$ presents a spike at the beginning of the short-circuit fault, which is due to the discharge of the LC-filter capacitor. After the fault, both currents return to their initial state smoothly.

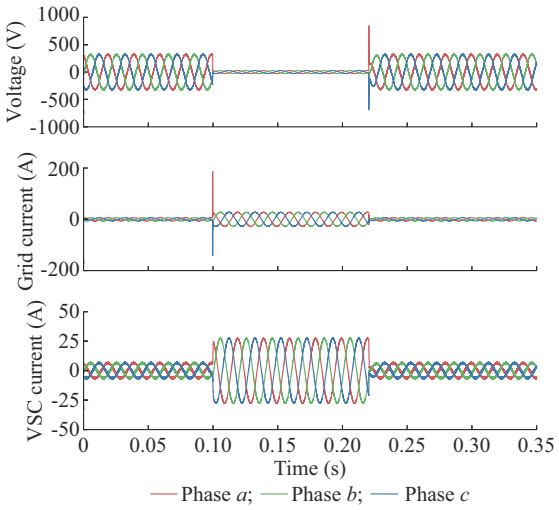

Fig. 11. HIL simulation of three-phase fault at PCC.

Therefore, it can be stated that the delay introduced by the state observer does not significantly affect the controller performance even in the case of a large perturbation.

V. Conclusion

This paper has presented a modification of the classic cascade voltage control which can be used as a part of the control algorithm of grid-forming VSCs with LC coupling filter operating in islanded mode. The proposed control algorithm allows to tune the gains of the OCL and ICL independently and easily. This has been achieved by introducing a virtual conductance in parallel with the coupling filter capacitor which turns the OCL plant as a first-order system if the ICL dynamics is neglected. It is worth noting that the simplified OCL plant is the dual circuit of the ICL one. As a consequence, both control loops can be designed in the same way following a straightforward strategy that, in addition, assures a controlled closed-loop dynamics.

This paper has introduced a sensitivity analysis to evidence the influence of two key parameters required to properly adjust the controller gains: the virtual conductance and the ICL time constant. For this purpose, frequency domain and stability analyses have been carried out. These analyses have been formulated following a per unit approach to obtain general conclusions independently of the rated values of the VSC. The main outcome that can be derived from the frequency domain analysis is that small virtual conductance values are preferred because of the large controller gains obtained in the low-frequency range where the controller is intended for. The stability analysis brings the same conclusion because small virtual conductance values lead to higher damping ratios and reduced resonance frequencies.

The proposal has been experimentally validated in a laboratory testbed where steady-state and transient regimes have been evaluated under load and no-load conditions. The results show that the proposed control algorithm obtains zero steady-state error and very low THD values with and without load. Regarding the transient results, the voltage follows a first-order dynamics with the time constant used in the definition of the controller gains. In addition to these experimental tests, an HIL testing approach has been applied in order to evidence that the delay introduced by the state observer of the inductor current does not significantly affect the controller dynamics even in the case of large perturbations.

Future research lines will incorporate to this cascade voltage controller new control layers dealing with key functionalities of grid-former VSCs for islanded systems like power sharing as well as unbalance and harmonic mitigations. In addition, it is expected to adapt the formulation to grid-forming VSCs operating in grid-connected mode.

Appendix A

A. State Observer for Inductor Current

The purpose of the state observer is to estimate the inductor current $\boldsymbol{i}_{t,dq}$ from the available measurements $\boldsymbol{i}_{s,dq}$ and $\boldsymbol{v}_{m,dq}$. The plant dynamics given by (3) and (4) is formulated in a compact form as:

$$\dot{\boldsymbol{x}}_p = \boldsymbol{A}_p \boldsymbol{x}_p + \boldsymbol{B}_p \boldsymbol{u}_p \tag{A1}$$

$$\boldsymbol{y}_p = \boldsymbol{C}_p \boldsymbol{x}_p \tag{A2}$$

where the subscript p is used to indicate the plant, $\boldsymbol{x}_p = [\boldsymbol{v}_{m,dq} \;\; \boldsymbol{i}_{t,dq}]^{\mathrm{T}}$ is the vector of state variables; $\boldsymbol{y}_p = \boldsymbol{v}_{m,dq}^{\mathrm{T}}$ is the system output vector; and $\boldsymbol{u}_p = [\boldsymbol{v}_{t,dq} \;\; \boldsymbol{i}_{s,dq}]^{\mathrm{T}}$ is the vector of system inputs.

By applying the Luenberger state observer definition over (A1) and (A2), (A3) and (A4) can be obtained [25]:

$$\dot{\tilde{\boldsymbol{x}}}_p = \boldsymbol{A}_p \tilde{\boldsymbol{x}}_p + \boldsymbol{B}_p \boldsymbol{u}_p + \boldsymbol{G}(\boldsymbol{y}_p - \tilde{\boldsymbol{y}}_p) \tag{A3}$$

$$\tilde{\boldsymbol{y}}_p = \boldsymbol{C}_p \tilde{\boldsymbol{x}}_p \tag{A4}$$

where $\tilde{\boldsymbol{x}}_p$ is the estimated vector state; $\tilde{\boldsymbol{y}}_p$ is the estimated output; $\boldsymbol{y}_p - \tilde{\boldsymbol{y}}_p$ is the estimation error; and $\boldsymbol{G}$ is the additional term called weighting matrix. This matrix, which defines the observer performance, can be computed by solving an LQR problem with the constraints imposed by (A1) and (A2). In this way, it is assured that the estimation error converges to zero. From a practical point of view, the LQR problem to compute $\boldsymbol{G}$ has been solved by using the MATLAB function *lqrd.m*. Once $\boldsymbol{G}$ is defined, it is possible to calculate the esti-

mated state vector $\tilde{\boldsymbol{x}}_p$ using (A3) and (A4). It is worth noting that the use of the current $\tilde{\boldsymbol{i}}_{t,dq}$ instead of the measured current $\boldsymbol{i}_{t,dq}$ improves the performance of the controller since the state observer also acts as a low-pass filter which eliminates the high-frequency harmonic content of the inductor current $\boldsymbol{i}_{t,dq}$ [8].

Matrices used in the state observer are defined as:

$$\boldsymbol{A}_p=\begin{bmatrix} 0 & \omega & 1/C & 0 \\ -\omega & 0 & 0 & 1/C \\ -1/L_t & 0 & -R_t/L_t & \omega \\ 0 & -1/L_t & -\omega & -R_t/L_t \end{bmatrix} \tag{A5}$$

$$\boldsymbol{B}_p=\begin{bmatrix} 0 & 0 & -1/C & 0 \\ 0 & 0 & 0 & -1/C \\ 1/L_t & 0 & 0 & 0 \\ 0 & 1/L_t & 0 & 0 \end{bmatrix} \tag{A6}$$

$$\boldsymbol{C}_p=\begin{bmatrix} 1 & 0 & 0 & 0 \\ 0 & 1 & 0 & 0 \end{bmatrix} \tag{A7}$$

B. Stability Analysis Matrices

Matrices $\boldsymbol{A}$ and $\boldsymbol{B}$ of the stability analysis outlined in Section III-B are presented as:

$$\boldsymbol{A}=\begin{bmatrix} a & 0 & b & c & d & 0 & e & 0 \\ 0 & a & -c & b & 0 & d & 0 & e \\ 1/C & 0 & 0 & \omega & 0 & 0 & 0 & 0 \\ 0 & 1/C & -\omega & 0 & 0 & 0 & 0 & 0 \\ -1 & 0 & f & C\omega & 0 & 0 & k_{i,v} & 0 \\ 0 & -1 & C\omega & f & 0 & 0 & 0 & k_{i,v} \\ 0 & 0 & -1 & 0 & 0 & 0 & 0 & 0 \\ 0 & 0 & 0 & -1 & 0 & 0 & 0 & 0 \end{bmatrix} \tag{A8}$$

$$\boldsymbol{B}=\begin{bmatrix} \dfrac{k_{p,v}k_{p,i}}{L_t} & 0 & \dfrac{k_{p,i}}{L_t} & 0 \\ 0 & \dfrac{k_{p,v}k_{p,i}}{L_t} & 0 & \dfrac{k_{p,i}}{L_t} \\ 0 & 0 & -1/C & 0 \\ 0 & 0 & 0 & -1/C \\ k_{p,v} & 0 & 1 & 0 \\ 0 & k_{p,v} & 0 & 1 \\ 1 & 0 & 0 & 0 \\ 0 & 1 & 0 & 0 \end{bmatrix} \tag{A9}$$

where terms a, b, c, d, e, and f are defined as: $a=\dfrac{-(k_{p,i}+R_t)}{L_t}$; $b=\dfrac{-k_{p,i}(G_v+k_{p,v})}{L_t}$; $c=\dfrac{-Ck_{p,i}\omega}{L_t}$; $d=\dfrac{k_{i,i}}{L_t}$; $e=\dfrac{k_{i,v}k_{p,i}}{L_t}$; and $f=-(G_v+k_{p,v})$.

REFERENCES

[1] J. M. Maza-Ortega, E. Acha, S. García *et al*., "Overview of power electronics technology and applications in power generation transmission and distribution," *Journal of Modern Power Systems and Clean Energy*, vol. 5, no. 4, pp. 499-514, Jul. 2017.

[2] S. H. Ko, S. R. Lee, H. Dehbonei *et al*., "Application of voltage- and current-controlled voltage source inverters for distributed generation systems," *IEEE Transactions on Energy Conversion*, vol. 21, no. 3, pp. 782-792, Sept. 2006.

[3] J. T. Bialasiewicz, "Renewable energy systems with photovoltaic power generators: operation and modeling," *IEEE Transactions on Industrial Electronics*, vol. 55, no. 7, pp. 2752-2758, Jun. 2008.

[4] T. Qoria, T. Prevost, G. Denis *et al*., "Power converters classification and characterization in power transmission systems," in *Proceedings of 2019 21st European Conference on Power Electronics and Applications*, Genova, Italy, Sept. 2019, pp. 1-6.

[5] J. Rocabert, A. Luna, F. Blaabjerg *et al*., "Control of power converters in AC microgrids," *IEEE Transactions on Power Electronics*, vol. 27, no. 11, pp. 4734-4749, Nov. 2012.

[6] P. Rodriguez, C. Citro, J. I. Candela *et al*., "Flexible grid connection and islanding of SPC-based PV power converters," *IEEE Transactions on Industry Applications*, vol. 54, no. 3, pp. 2690-2702, May 2018.

[7] G. N. Baltas, N. B. Lai, L. Marin *et al*., "Grid-forming power converters tuned through artificial intelligence to damp subsynchronous interactions in electrical grids," *IEEE Access*, vol. 8, pp. 93369-93379, May 2020.

[8] J. C. Olives-Camps, J. M. Mauricio, M. Barragan-Villarejo *et al*., "Voltage control of four-leg VSC for power system applications with nonlinear and unbalanced loads," *IEEE Transactions on Energy Conversion*, vol. 35, no. 2, pp. 640-50, Jun. 2020.

[9] R. Perez-Ibacache, G. A. Pimentel, C. A. Silva *et al*., "State feedback control with full disturbance compensation for an LC filtered grid-forming converter," in *Proceedings of 2019 IEEE PES Innovative Smart Grid Technologies Conference – Latin America (ISGT Latin America)*, Gramado, Brazil, Sept. 2019, pp. 1-6.

[10] T. Qoria, C. Li, K. Oue *et al*., "Direct AC voltage control for grid-forming inverters," *Journal of Power Electronics*, vol. 20, no. 1, pp. 198-211, Dec. 2019.

[11] P. C. Loh and D. G. Holmes, "Analysis of multiloop control strategies for LC/CL/LCL-filtered voltage-source and current-source inverters," *IEEE Transactions on Industry Applications*, vol. 41, no. 2, pp. 644-654, Mar. 2005.

[12] Q. Lei, F. Peng, and S. Yang, "Multiloop control method for high-performance microgrid inverter through load voltage and current decoupling with only output voltage feedback," *IEEE Transactions on Power Electronics*, vol. 26, no. 3, pp. 953-960, Dec. 2011.

[13] Z. Li, C. Zang, P. Zeng *et al*., "Control of a grid-forming inverter based on sliding-mode and mixed H_2/H_∞ control," *IEEE Transactions on Industrial Electronics*, vol. 64, no. 5, pp. 3862-3872, May 2017.

[14] T. Qoria, F. Gruson, F. Colas *et al*., "Tuning of cascaded controllers for robust grid-forming voltage source converter," in *Proceedings of 20th Power Systems Computation Conference*, Dublin, Ireland, Aug. 2018, pp. 1-7.

[15] Z. Li, C. Zang, P. Zeng *et al*., "Analysis of multi-agent-based adaptive droop-controlled AC microgrids with PSCAD: modeling and simulation," *Journal of Power Electronics*, vol. 15, no. 2, pp. 455-468, Mar. 2015.

[16] T. Qoria, F. Gruson, F. Colas *et al*., "Critical clearing time determination and enhancement of grid-forming converters embedding virtual impedance as current limitation algorithm," *IEEE Journal of Emerging and Selected Topics in Power Electronics*, vol. 8, no. 2, pp. 1050-1061, Dec. 2019.

[17] D. Pan, X. Wang, F. Liu *et al*., "Transient stability of voltage-source converters with grid-forming control: design-oriented study," *IEEE Journal of Emerging and Selected Topics in Power Electronics*, vol. 8, no. 2, pp. 1019-1033, Jun. 2020.

[18] Y. Y. Tzou, "DSP-based fully digital control of a PWM DC-AC converter for AC voltage regulation," in *Proceedings of PESC Record – IEEE Annual Power Electronics Specialists Conference*, Atlanta, USA, Jun. 1995, pp. 138-144.

[19] V. Yaramasu, M. Rivera, M. Narimani *et al*., "Model predictive approach for a simple and effective load voltage control of four-leg inverter with an output LC filter," *IEEE Transactions on Industrial Electronics*, vol. 61, no. 10, pp. 5259-5270, Oct. 2014.

[20] J. W. Jung, V. Q. Leu, D. Dang *et al*., "Intelligent voltage control strategy for three-phase UPS inverters with output LC filter," *International Journal of Electronics*, vol. 102, no. 8, pp. 1267-1288, Aug. 2015.

[21] Y. Li, Y. Gu, Y. Zhu *et al*., "Impedance circuit model of grid-forming inverter: visualizing control algorithms as circuit elements," *IEEE Transactions on Power Electronics*, vol. 36, no. 3, pp. 3377-3395, Mar. 2021.

[22] A. Yazdani and R. Iravani, *Voltage-sourced Converters in Power Systems: Modeling, Control, and Applications*. New York: John Wiley, Jan. 2010.

[23] F. Briz, D. Díaz-Reigosa, M. W. Degner *et al*., "Current sampling and measurement in PWM operated AC drives and power converters," in

Proceedings of 2010 International Power Electronics Conference, Sapporo, Japan, Jun. 2010, pp. 2753-2760.
[24] H. Markaroglu, M. Guzelkaya, I. Eksin *et al*., "Tracking time adjustment in back calculation anti-windup scheme," in *Proceedings of 20th European Conference on Modelling and Simulation ECMS 2006: Modelling Methodologies and Simulation: Key Technolgies in Academia and Industry*, Bonn, Germany, May 2006, p. 613.
[25] D. G. Luenberger, "An introduction to observers," *IEEE Transactions on Automatic Control*, vol. 16, no. 6, pp. 596-602, Dec. 1971.

Francisco Jesús Matas-Díaz received the aerospace engineering degree and the Master degree in power systems from the University of Seville, Seville, Spain, in 2017 and 2020, respectively, where he is currently a Ph.D. student and Research Assistant at the Department of Electrical Engineering. His research interests include microcontroller programming, hardware-in-the-loop (HIL) simulations, and power converters experimental validation.

Manuel Barragán-Villarejo received the bachelor and Ph. D. degrees in electrical engineering from the University of Seville, Seville, Spain, in 2008 and 2014, respectively. Since 2008, he has been with the Department of Electrical Engineering, University of Seville, where he is currently an Associate Professor. His research interests include exploitation and control of power converters for smart grid management and grid integration of distributed renewable energy sources.

Juan Carlos Olives-Camps received the bachelor degree from the Technical University of Catalonia (UPC), Barcelona, Spain, in 2014, and the master degree from University of Seville, Seville, Spain, in 2018, both in electrical engineering. He is currently working toward the Ph.D. degree at the Department of Electrical Engineering, University of Seville. His research interests include power systems control, voltage source converter-based applications, and renewable energy integration.

Juan Manuel Mauricio received the bachelor degree in electrical engineering from the National University of Comahue, Neuquen, Argentina, in 2003, and the master and doctor Engineering degrees from the University of Seville, Seville, Spain, in 2007 and 2009, respectively. Since 2004, he has been with the Department of Electrical Engineering, University of Seville, where he is currently an Associate Professor. His research interests include power systems and electrical machine control, renewable generation, voltage source converter-based applications, and electrical vehicles.

José María Maza-Ortega received the bachelor degree in electrical engineering and Ph.D. degree from the University of Seville, Seville, Spain, in 1996 and 2001, respectively. Since 1997, he has been with the Department of Electrical Engineering, University of Seville, where he is currently an Associate Professor. His research interests include power quality, harmonic filters, integration of renewable energies, and power electronics.